

Photometric Calibration and Elevation-Dependent Atmospheric Correction in Multistatic Light Curve Analysis

Manik Reichegger ⁽¹⁾, Anja Schlicht ⁽¹⁾, Johann Eckl ⁽²⁾, Urs Hugentobler ⁽¹⁾

⁽¹⁾ Chair of Satellite Geodesy, Technical University of Munich, Arcisstraße 21, 80333 Munich, Germany

⁽²⁾ Federal Agency for Cartography and Geodesy, Sackenrieder Straße 25, 93444 Bad Kötzing, Germany

manik.reichegger@tum.de, johann.eckl@bkg.bund.de, anja.schlicht@tum.de, urs.hugentobler@tum.de

ABSTRACT

The increasing amount of space debris poses a major collision risk in Earth's orbit. The retrieval of objects from orbit, and therefore the assessment of an object's orientation, is crucial for risk mitigation. Variations in observed brightness, resulting from reflected sunlight, provide insights into an object's rotational parameters. To enhance orientation determination, additional observatories must participate in the measurements, ensuring their brightness values are comparable. This study focuses on developing a calibration process for multistatic light curve analysis. The analysis combines two methods: The first employs plate solving to convert instrument-dependent brightness values into standardized magnitudes using stellar images matched with the Gaia catalogue. The second examines extinction effects by observing spherical satellites with known phase angles, deriving atmospheric and instrumental corrections from the comparison of theoretical backscatter and observed brightness. These corrections then allow the calibration dataset to be used to estimate the albedo of the observed object.

1 INTRODUCTION

The growing accumulation of space debris significantly increases the likelihood of collisions between objects in orbit. To mitigate this risk, the retrieval of objects from orbit is essential. A crucial factor in this process is assessing an object's orientation. During an object's pass, variations in observed brightness result from changing sunlight reflections to the observer. Analyzing these variations over time provides insights into the object's rotational parameters and attitude.

To enhance orientation determination of space debris, a network of measurement stations can provide supplementary data. [1] However, it is essential to ensure comparability between different observations made with different equipment and under different conditions. Differences in camera characteristics, telescope optics, and atmospheric conditions can influence the recorded brightness values, potentially leading to inconsistencies.

The objective of this study is to develop a standardised

calibration procedure for multistatic light curve analysis. The establishment of a method for converting relative brightness values to a comparable scale will facilitate the comparison of measurements and ensure the benefits of cooperative analysis. In a subsequent step, where conclusions about the shape or surface parameters of the observed object are to be drawn, these standardised measurements are essential for the processing of the data provided by the participating observatories.

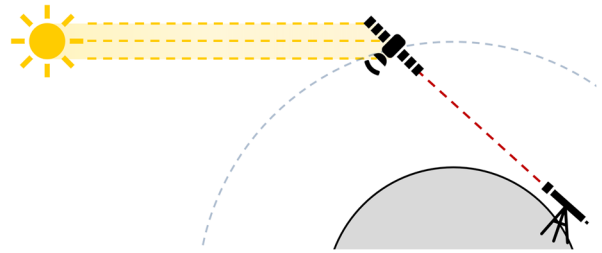


Figure 1. Passive optical observation geometry of an orbital debris object.

The object must be illuminated by the Sun while the observer remains in Earth's shadow, restricting observation windows to a short period after sunset and before sunrise, depending on the object's orbital height.

To achieve this comparability, we utilize the well-established plate solving method, which employs known reference stars for calibration. This method was utilised in order to perform a comparative analysis. An alternative approach was explored by calibrating the observations with the theoretically derived photon flux from spherical satellites. This dual-calibration strategy enables a comprehensive assessment of measurement accuracy and ensures robust photometric standardization across different observatories. Furthermore, a combination of the two methods offers an improved possibility of determining the average albedo of an observed object, if the equipment-specific and weather-dependent parameters have already been determined and the attitude and orbit of the object are sufficiently known. The present study focuses on the analysis of spherical satellites due to the absence of any influence on their attitude as a consequence of their quasi-homogeneous surface.

Chapter 2.1 - 2.3 outlines the methodology, covering image calibration, photon flux determination, and extinction corrections to ensure consistent photometric measurements. Chapter 2.4 presents the results, comparing the plate solving and spherical satellite calibration methods and their impact on measurement accuracy. Chapter 3 focuses on combining these methods to establish consistent and comparable measurements across observatories, enabling albedo estimation when observational conditions are well known. The outlook discusses future observations of objects with well-characterized albedo and how the derived parameters could be integrated into forward simulations.

2 METHODOLOGY AND RESULTS

2.1 Image Calibration

To minimize systematic errors introduced by the optical system, image calibration is a fundamental step in astronomical image processing, ensuring the correction of sensor-related noise and optical distortions. This process begins with the application of a master dark frame, which compensates for thermal noise generated by the camera sensor. Since each pixel produces a small signal even in the absence of light, multiple dark exposures are averaged to create a reference frame that is then subtracted from the raw images. Next, a master bias frame is applied to remove readout noise, which originates from the camera's electronics during the image recording process. This correction eliminates unwanted electronic offsets, improving the accuracy of faint signal measurements. Finally, a flat-field correction is performed using a master flat frame, which compensates for pixel sensitivity variations and optical vignetting. This is achieved by imaging a uniformly illuminated field, such as a twilight sky or a specially designed flat-field screen, and normalizing the science images accordingly. [2]

2.2 Determination of the Photon Flux from the Observations

For accurately extracting light curves from astronomical observations, aperture photometry plays a crucial role in measuring the brightness and its variations of celestial objects. The process involves automated tracking of the light source's centre in each frame to ensure precise brightness measurements. To perform this extraction, three key regions around the tracked centre are considered: the core or diffraction disk, which contains 90% of the total light, the aureole, holding 90% of the remaining light, and the surrounding sky, which includes background stars and a minor fraction of scattered light. For the calculation two primary measurement regions are defined: the aperture (core + aureole), capturing the star and background with $2.8 \times \text{HWHM}$, and the annular background region, representing only the background

with $4 \times \text{HWHM}$. To isolate the true stellar signal, the annular background subtraction method is applied, ensuring that background contributions are removed. [3] The HWHM (Half-Width at Half-Maximum) is determined individually for each equipment based on a point light source.

The resulting total pixel value sum is stored as Analog-to-Digital Units (ADUs) and subsequently converted into photon flux using camera and telescope parameters.

$$\text{PhotonFlux} = \frac{ADU * \text{Gain}}{QE * \text{ExposureTime} * \text{TelescopeArea}} \quad (1)$$

Eq. 1 [4] describes the conversion of Analog-to-Digital Units (*ADU*) into Photon Flux, considering various instrumental parameters that influence the recorded signal. *ADU* represents the raw pixel values captured by the camera, which are converted into electrons using the gain factor, a parameter specific to the camera's electronics. The quantum efficiency (*QE*) defines the sensor's ability to convert incident photons into electrons. The *ExposureTime* defines the duration over which light is collected, determining the total number of detected photons, while the *TelescopeArea* represents the effective collecting area of the telescope, influencing the number of incoming photons reaching the detector. By normalizing *ADU* values with these factors, the equation provides the absolute Photon Flux arriving at the telescope.

2.3 Determination of Extinction Parameters

To ensure the comparability of measurements obtained from different observing stations using various equipment and located in diverse atmospheric conditions, it is essential to quantify and correct for all influencing parameters. One key factor is the elevation-dependent atmospheric extinction, which affects the observed brightness as a function of the air mass through which the light passes. A greater distance from the zenith results in a longer path through the atmosphere. Additionally, there is also an elevation-independent constant extinction which affects the incoming light. Both parameters are influenced by local weather conditions, including temperature, humidity, dust, and observatory altitude.

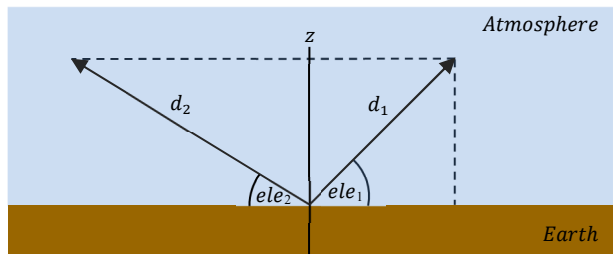


Figure 2. The figure illustrates the simplest atmospheric model, a single-layer plane approximation. Zenith represented by z , while d_1 and d_2 denote the elevation-dependent distances at the same orbital height.

Furthermore, the transmission efficiency of the telescope optics must be accounted for, as optical coatings and material properties influence the total collected light. The camera sensor characteristics, including non-idealities not explicitly stated in the manufacturer's datasheet, introduce additional uncertainties. The presence of scattered light at the observatory location, caused by artificial or natural sources, can also impact photometric accuracy.

It is crucial to precisely determine these extinction factors, which include atmospheric variations, instrumental systematics, and other influencing parameters, to ensure the accuracy and comparability of the measurements. Therefore, the next sections deal with the implementation of a robust and standardised calibration procedure that can be performed by the stations to allow a reliable quantification of these effects and to ensure a consistent and comparable multistatic photometric analysis of objects in orbit.

2.3.1 Plate Solving Methodology

Plate solving is a computational method used to determine the precise celestial coordinates of an astronomical image by matching star patterns with known catalogues. Astrometry.net automates this process using a quad-based pattern recognition algorithm. It first detects bright sources in an image, extracts characteristic star patterns, and compares them to indexed reference catalogues such as Gaia or Tycho-2. Once a match is found, a World Coordinate System (WCS) solution is computed, mapping pixel positions to celestial coordinates. This method enables accurate image calibration, ensuring consistency across different observatories. [5]

In this study, the Gaia DR3 catalogue is employed to calibrate the recorded brightness values by converting the measured Analog-to-Digital Units into photon flux by applying Eq. 1. This calibrated flux is then compared with the Gmag magnitude from Gaia to derive a conversion function, ensuring accurate and consistent photometric measurements.

$$Mag = -2,5 * \log_{10}(PhotonFlux) - Gaia_zeropoint - \left(k_0 + k * \left(\frac{1}{\sin(ele)} \right) \right) \quad (2)$$

k_0 ... elevation independent component

k ... elevation dependent component

The first term of Eq. 2 represents the instrumental magnitude according to Campbell et al. [4], derived from the logarithmic conversion of the measured photon flux. The *Gaia zeropoint*, a calibration factor given by Lang et. al [5], is then applied to adjust instrumental magnitudes to a standardized system. It corrects the converted photon flux to match the Gaia magnitude

system, accounting for instrumental differences and ensuring alignment with the standard scale.

The final term of Eq. 2 is based on the Bouguer-Lambert-Beer law, which describes the reduction in radiation intensity as it passes through an absorbing medium and is further derived in Eq. 3.

$$E_\lambda = \log_{10} \left(\frac{I_0}{I_1} \right) = \varepsilon_\lambda * c * d = k_\lambda * d \quad (3)$$

where $d = 1 / \sin(ele)$

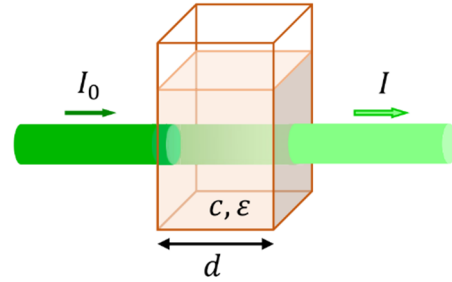


Figure 3. Illustration of Beer-Lambert-Bouguer law: Transmission of light through a sample medium. Reproduced from [7], licensed under CC BY 4.0

The intensity of transmitted light (I_1) is influenced by the initial incident light intensity (I_0) as it passes through an absorbing medium. This attenuation is governed by the spectral absorption coefficient (ε_λ), which describes the material's wavelength-dependent absorption properties. Additionally, the mass concentration of the absorbing substance (c) and the thickness of the irradiated medium (d) determine the overall reduction in light intensity.

In this context, we consider two types of extinction. The parameter k_0 represents the elevation-independent extinction, incorporating all factors that do not vary with observation elevation. This includes the previously mentioned telescope and camera characteristics, atmospheric influences at the zenith, as well as the difference in sensor sensitivity between our equipment and the Gaia reference magnitudes due to variations in wavelength response. The parameter k , on the other hand, quantifies the elevation-dependent dimming of starlight caused by Earth's atmosphere, as illustrated in Fig. 2. This effect is primarily due to scattering and absorption by atmospheric molecules and particles. Unlike k_0 , this factor is elevation-dependent, as it is directly influenced by the air mass, which is a function of the observation's elevation angle (Eq. 2).

The result of the plate solving method (instrument magnitudes against corresponding Gaia magnitudes) shown in Fig. 4 is reduced using a 3σ clipping method to eliminate outliers. For the filtered data, a linear fit is applied based on Eq. 2, enabling the estimation of the elevation-independent factor k_0 and the elevation-dependent factor k , which are necessary for correcting atmospheric and instrumental influences.

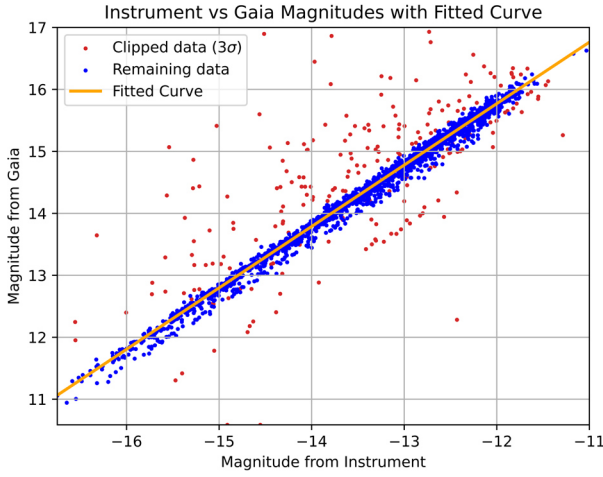


Figure 4. Result of the plate solving method. The X-axis represents the instrumental magnitude calculated using the first term of Eq. 2, while the Y-axis shows the corresponding G_{mag} from the Gaia DR3 catalogue.

In the two plots, Fig. 5 and Fig. 6, the same measured dataset is displayed again, this time with data points color-coded according to elevation. Fig. 5 shows a noticeable spread of the data, which highlights the influence of elevation in the measurements. At this stage, neither k nor k_0 has been applied. Only the first term from Eq. 2 ($-2,5 * \log_{10}(PhotonFlux)$) was used to convert the flux into a magnitude.

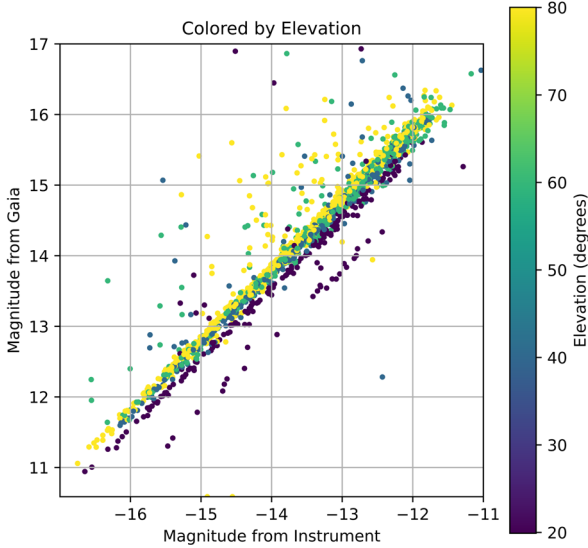


Figure 5. Result of the plate solving method, where the data were converted into magnitudes using only the first term of Eq. 2, with the data points color-coded according to their elevations. (Conversion identical to Fig. 4)

When applying the two estimated parameters and transforming the data points using the corresponding k_0

and k , the corrected result is shown in Fig. 6. Compared to Fig. 5, a clear compression of the data can be observed, effectively reducing the spread caused by elevation-dependent extinction. This demonstrates that the applied correction successfully compensates for atmospheric effects, making the measurements more consistent and elevation-independent.

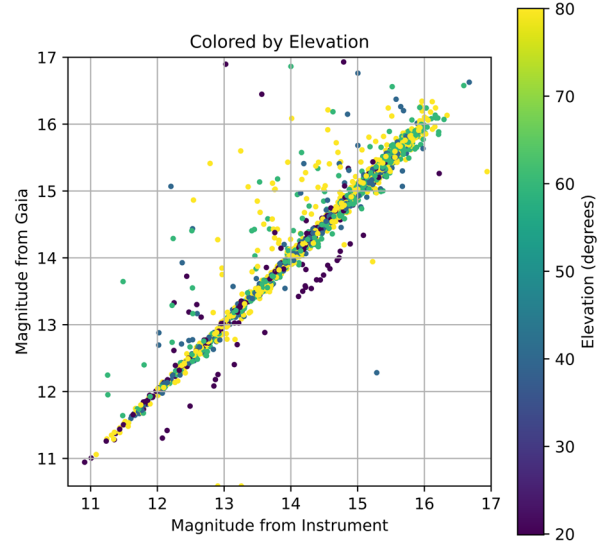


Figure 6. Result of the plate solving method, where the data has been converted to Gaia magnitudes using Eq. 2 with the estimated k_0 and k . The data points are color-coded according to their elevations.

Additionally, after applying the transformation function, the instrumental magnitude now aligns with the Gaia magnitude in Fig. 6, ensuring that all data points are on the same scale.

2.3.2 Spherical Satellite Methodology

As an alternative approach to plate solving, we observed several spherical satellites with relatively homogeneous surface properties during their passes. These satellites were chosen because their well-known orbits minimize positional uncertainties, and their nearly uniform surfaces ensure that attitude errors have little to no impact on brightness measurements. In this initial step, the satellites were modelled as Lambertian emitters, providing a first-order approximation of their reflective properties. The known phase angle, defined as the angle between the light source, observer, and object, serves as a basis for estimating the theoretical brightness of the satellite as perceived by the observer. By comparing this theoretical backscatter with the observed brightness, we can quantify elevation-dependent atmospheric effects and apply these corrections to other measurements within the same campaign. Similar to the plate solving method, this approach introduces both an elevation-dependent and an elevation-independent coefficient. [8]

Phase function:

$$f(\phi) = \frac{2}{3\pi^2} [\sin(\phi) + (\pi - \phi) \cos(\phi)] \quad (4)$$

Theoretical Flux:

$$F_{app}(\nu) = \frac{\pi d^2}{4R^2} \alpha_g f(\phi) F_{sun}(\nu) * 10^{-0,4*(k_0+k \frac{1}{\sin(ele)})} \quad (5)$$

Eq. 4 [9] describes the Lambertian phase function used for the theoretical calculations, even though it is known that, in the case of orbital debris, the phase function is a complex combination of specular and Lambertian components.

In Eq. 5 [9], the formula for the theoretically observed flux is provided, applying Eq. 4 as a Lambertian emitter, specifically for the case of a spherical object.

The final term in Eq. 5, expressed as $10^{-0,4*(k_0+k \frac{1}{\sin(ele)})}$, accounts for the atmospheric attenuation of light as it propagates through Earth's atmosphere. This attenuation, already discussed in Eq. 2, is primarily caused by Beer-Lambert-Law Eq. 3, which describes the transmission of light through a sample medium.

Derivation of the extinction correction in the calculation of the photon flux:

$$-2,5 * \log_{10}(Flux_{obs}) = -2,5 * \log_{10}(PhotonFlux_{true}) + A \quad (6)$$

$$\log_{10}(Flux_{obs}) = \log_{10}(Flux_{true}) + \frac{A}{2,5} \quad (7)$$

$$Flux_{obs} = Flux_{true} * 10^{-0,4A} \quad (8)$$

$$where A = \left(k_0 + k * \left(\frac{1}{\sin(ele)} \right) \right)$$

Similar to the plate solving method, this approach introduces two coefficients that need to be determined: the elevation-independent coefficient k_0 accounts for various factors, including molecular absorption at zenith, as well as instrumental effects such as filter and telescope transmission efficiency, camera sensor sensitivity, and other system-specific influences that remain constant regardless of the observation angle. In contrast, the elevation-dependent coefficient k accounts for the increased optical path length through the atmosphere at lower elevation angles, which enhances extinction. The air mass term $1/\sin(ele)$ represents the relative amount of atmosphere the light must traverse, increasing as the observation moves away from zenith (Fig. 2).

However, it is important to note that the k_0 determined using this method differs from the k_0 obtained via the plate solving approach. In plate solving, all magnitudes are referenced to the Gaia Gmag magnitudes and its specific filter properties and sensor characteristics. In contrast, this approach relies on the theoretical backscattered brightness of the satellite calculated with a mean $F_{sun}(\nu)$.

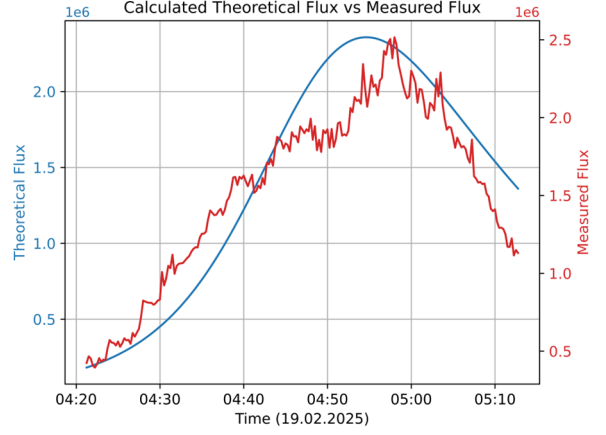


Figure 7. Theoretically calculated flux (blue) for a pass of LAGEOS-1 over Wettzell on February 19, 2025, alongside the corresponding measured photon flux (red) Equipment: QHY 174 GPS CMOS / PlaneWave CDK 14

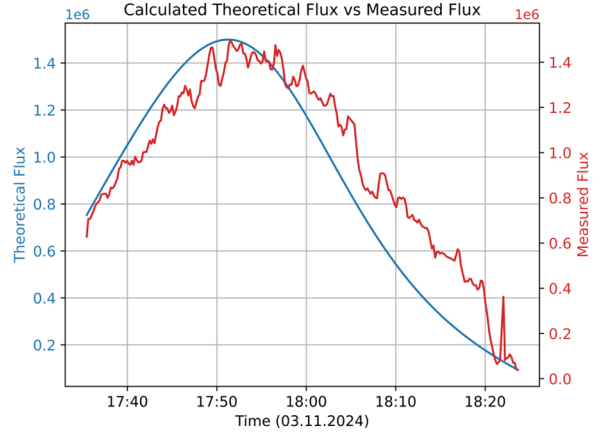


Figure 8. Theoretically calculated flux (blue) for a pass of LAGEOS-1 over Wettzell on November 03, 2024, alongside the corresponding measured photon flux (red) Equipment: ASI ZWO 1600 MM Pro CMOS / PlaneWave CDK 14

Since k_0 and the albedo are not directly separable in this method, both parameters cannot be determined simultaneously, and one must be known in advance.

A first approach is to observe an object with a well-known albedo and determine k_0 and k independently of the plate solving method. However, in this case, the coefficients cannot be directly verified against those from the plate solving, as they are referenced to entirely different scales.

This method can be reliably used as an independent calibration approach, provided that the reflection parameters of the observed object are sufficiently well known. The advantage of this would be a significantly lower computational effort compared to plate solving.

2.4 Combination of the Methods and Determination of Albedo

When combining the two calibration methods, we follow two approaches.

The first approach is to adopt the coefficients k_0 and k from the plate solving method to determine the albedo of a specific spherical object with Eq. 5. This albedo would then be referenced to the Gaia Gmag system, incorporating the sensor and filter characteristics of both the Gaia instrumentation and the equipment used in the plate solving process.

In the future, this object, with its determined albedo, can be used to recalibrate and derive the extinction coefficients k_0 and k , ensuring a consistent and iterative refinement of atmospheric correction parameters without plate solving.

In the second approach, the objective remains the determination of surface properties. However, this method employs as a first step an object with a well-characterized albedo to derive both extinction coefficients, k_0 and k , similar to the method described in Section 2.3.2 Spherical Satellite Methodology. In a subsequent step of the same measurement campaign, k_0 and k are determined using plate solving.

To reconcile the two approaches, we introduce a Δk_0 correction factor, which serves as a constant conversion offset between our instrumental system and Gaia's reference system. Unlike the plate solving approach, the spherical satellite method does not rely on Gaia's Gmag as a reference, meaning that the obtained value for k_0 will naturally differ from those derived using the plate solving technique. To ensure consistency across the different calibration methods and establish a unified correction framework that accounts for both instrumental and atmospheric influences, this correction Δk_0 is applied.

$$\Delta k_0 = k_{0\text{PlateSolving}} - k_{0\text{SphericalSatellites}} \quad (8)$$

By incorporating the calculated Δk_0 into our theoretical photon flux equation and using k_0 and k from plate solving, we can account for the systematic offset between our measurement magnitudes and the Gaia reference magnitudes. This allows us to determine the instrument-dependent average albedo for all observed objects under the given measurement conditions.

$$F_{app}(v) = \frac{\pi d^2}{4R^2} \alpha_g f(\phi) F_{sun}(v) * 10^{-0.4 * ((k_0 - \Delta k_0) + k \frac{1}{\sin(\epsilon)})} \quad (9)$$

In addition, the calculated Δk_0 can be used to adjust the plate-solving method by removing the Gaia-specific component, ensuring a more generalized calibration framework.

The correction factor Δk_0 compensates for differences

between the plate-solving calibration (Gaia Gmag reference) and the spherical satellite method (theoretical flux reference). Without this correction, comparisons between the two methods would be biased due to their reliance on different reference magnitudes. Applying this correction enhances consistency across both methods and improves the accuracy of object property determinations, such as albedo.

By implementing the second strategy and combining real measurements of LAGEOS-1 with the corresponding plate-solving data obtained on November 3rd in Wettzell, we are able to compute a value for Δk_0 specific to the instrumentation used. This calculation, however, relies on an assumed albedo for the observed satellite. In our dataset, an albedo of 0.35 is considered for LAGEOS-1, which is purely an assumption based on its structural design and the materials used.

The calculated Δk_0 allows us to estimate the albedo of LAGEOS-2 using Eq. 9, which was observed on November 4th, 2024. This assumption would yield an albedo of 0.6 for LAGEOS-2 based on the measurements from the following day. However, this value appears to be somewhat high, which may be attributed to the fact that the estimated albedo is directly dependent on the assumed albedo of LAGEOS-1 from the first pass, which was not sufficiently well known in this case. Any incorrect assumption about the albedo in the first pass directly affects the second derived parameter.

Moreover, the analysis may have been affected by suboptimal weather conditions and changing atmospheric conditions, which could introduce additional uncertainties. Given the limited number of available measurements and these external influencing factors, we are currently unable to make definitive statements regarding the accuracy and reliability of this measurement.

3 CONCLUSION AND OUTLOOK

The primary goal of this procedure is to establish consistent and comparable measurements across different observatories, ensuring that all observations are aligned to a uniform and standardized photometric scale. To do this, it is essential to reduce instrumental and site-specific biases to allow cross-comparisons of brightness measurements from different locations and setups.

The two methods provide an independent approach to calibrating measurements across different observatories. Additionally, after introducing Δk_0 , a combination of both methods becomes possible, allowing for verification of the applied calibration.

When the observational conditions are well-characterized, the shown method enables the determination of backscatter coefficients, such as the albedo of observed objects. This approach contributes to

a deeper understanding of the surface properties and material composition of objects in orbit, which is crucial for both scientific studies and space situational awareness applications.

Unfortunately, our existing datasets are not sufficient to reliably validate the developed methods. We are currently in the process of collecting additional data to confirm our approach. An important aspect of our ongoing work is also the further development and refinement of our methodologies. This includes, for example, improving the physical modelling of atmospheric effects by moving beyond the simple $1/\sin(ele)$ approximation and considering more realistic radiative properties of the satellite. Instead of treating the satellite as a purely Lambertian emitter, we aim to develop a more advanced physical radiation model that better reflects its actual optical characteristics.

As a future outlook, we plan to further test this method with various spherical satellites and verify the proposed approaches. In this context, we aim to observe the Lincoln Calibration Sphere (LCS), a homogeneous hollow aluminum sphere used for the calibration of ground-based radars. The well-defined surface properties of the LCS make it an ideal candidate for this validation.

As a final step, the derived parameters, including the corrected extinction coefficients (k_0 and k) and the adjusted albedo values, can be integrated into our forward simulation of light curves. This simulation models the expected brightness variations of an observed object over time, considering factors such as its rotational dynamics, surface properties, and illumination conditions. By incorporating the calibrated parameters, the simulation can more accurately predict how light is reflected and scattered from the object as it moves through different viewing geometries.

4 ACKNOWLEDGEMENTS

Gefördert durch:



Bundesministerium
für Wirtschaft
und Klimaschutz

aufgrund eines Beschlusses
des Deutschen Bundestages

The authors would like to express their sincere gratitude to the Bundesministerium für Wirtschaft und

Klimaschutz (BMWK) for funding this research under Grant No. 50LZ2204 for the project "Multistatische Lichtkurven: Analyse der Komplementarität der Messinformation."

We also acknowledge the Technische Universität München – Forschungseinrichtung Satellitengeodäsie for their support and access to essential resources. Special thanks go to our colleagues and collaborators for their valuable discussions and contributions to the analysis.

Furthermore, we would like to thank the staff of the Geodetic Observatory Wettzell and the Bundesamt für Kartographie und Geodäsie (BKG) for their invaluable support and for providing access to their equipment, which was essential for this study.

5 REFERENCES

1. Wang, Z., Schlicht, A., Reichegger, M. & Hugentobler, U. (2025). Attitude Observability based on Simulated Multiple Light Curve Observations from a Single Facet Target, *9th European Conference on Space Debris*, Bonn, Germany
2. Berry, R. & Burnell, J. (2000). *The Handbook of Astronomical Image Processing*, Willmann-Bell, Richmond, VA, USA, pp. 119–155.
3. Berry, R., & Burnell, J. (2000). *The Handbook of Astronomical Image Processing*, Willmann-Bell, Richmond, VA, USA, pp. 187–189.
4. Campbell, T.; Battle, A.; Gray, D.; Chabra, O.; Tucker, S.; Reddy, V.; Furfaro, R. (2024). Stingray Sensor System for Persistent Survey of the GEO Belt. *Sensors*, vol. 24, no. 8, p. 2596. <https://doi.org/10.3390/s24082596>
5. Lang, D., Hogg, DW, Mierle, K., Blanton, M., & Roweis, S., (2010). Astrometry.net: Blind astrometric calibration of arbitrary astronomical images. *The Astronomical Journal*, vol. 139, no. 5, pp. 1782-1800 <https://doi.org/10.1088/0004-6256/139/5/1782>
6. Riello, M., De Angeli, F., Evans, D. W., Montegriffo, P., Carrasco, J. M., Busso, G., Palaversa, L., Burgess, P. W., Diener, C., Davidson, M., Rowell, N., Fabricius, C., Jordi, C., Bellazzini, M., Pancino, E., Harrison, D. L., Cacciari, C., van Leeuwen, F., Hambly, N. C., Hodgkin, S. T., Osborne, P. J., Altavilla, G., Barstow, M. A., Brown, A. G. A., Castellani, M., Cowell, S., De Luise, F., Gilmore, G., Giuffrida, G., Hidalgo, S., Holland, G., Marinoni, S., Pagni, C., Piersimoni, A. M., Pulone, L., Raggini, S., Rainer, M., Richards, P. J., Sanna, N., Walton, N. A., Weiler, M., & Yoldas, A. (2021). Gaia Early Data Release 3: Photometric content and validation. *Astronomy & Astrophysics*, vol. 649, A3. <https://doi.org/10.1051/0004-6361/202039587>
7. Oshina, I. & Spigulis, J. (2021). Beer–Lambert law for

optical tissue diagnostics: current state of the art and the main limitations. *Journal of Biomedical Optics*, vol. 26, no. 10

<https://doi.org/10.1117/1.JBO.26.10.100901>

Licensed under CC BY 4.0

8. Hostetler, J. & Cowardin, H. (2019). Experimentally-Derived Phase Function Approximations in Support of the Orbital Debris Program Office, In *Proceedings of the 2019 International Orbital Debris Conference (IOC)*, Sugar Land, TX, USA, 2019
9. Barker, E., et al. (2004). Analysis of Working Assumptions in the Determination of Populations and Size Distributions of Orbital Debris from Optical Measurements, In *Proceedings of the 2004 AMOS Technical Conference*, Wailea, Maui, HI, pp. 225-235

For language refinement and readability improvements, AI-assisted tools (such as OpenAI's ChatGPT) were used. However, all scientific content, data interpretation, and conclusions were formulated independently by the authors.